Hyperfine structure and isotope shifts of the $(4s^2)\,^1S_0 \to (4s4p)\,^1P_1$ transition in atomic zinc

David Röser,[1,*] J. Eduardo Padilla-Castillo ®,[2,*] Ben Ohayon ®,[3] Russell Thomas ®,[2] Stefan Truppe ®,[2,4]
Gerard Meijer ®,[2] Simon Stellmer ®,[1] and Sid C. Wright ®[2,†]

[1]*University of Bonn, Nussallee 12, 53115 Bonn, Germany*
[2]*Fritz-Haber-Institut der Max-Planck-Gesellschaft, Faradayweg 4-6, 14195 Berlin, Germany*
[3]*The Helen Diller Quantum Center, Department of Physics, Technion-Israel Institute of Technology, Haifa 3200003, Israel*
[4]*Centre for Cold Matter, Blackett Laboratory, Imperial College London, London SW7 2AZ, United Kingdom*

We report absolute frequency, isotope shift, radiative lifetime, and hyperfine structure measurements of the $(4s^2)\,^1S_0 \to (4s4p)\,^1P_1$ (213.8 nm) transition in Zn I using a cryogenic buffer gas beam. Laser-induced fluorescence is collected with two orthogonally oriented detectors to take advantage of differences in the emission pattern of the isotopes. This enables a clear distinction between isotopes whose resonances are otherwise unresolved, and a measurement of the ^{67}Zn hyperfine structure parameters, $A(^{67}\mathrm{Zn}) = 20(2)\,\mathrm{MHz}$ and $B(^{67}\mathrm{Zn}) = 10(5)\,\mathrm{MHz}$. We reference our frequency measurements to an ultralow expansion cavity and achieve an uncertainty at the level of 1 MHz, about 1 percent of the natural linewidth of the transition.

I. INTRODUCTION

The alkaline-earth-metal (AEM) elements are identified by two valence electrons and a $J = 0$ electronic ground state. These two features give rise to a number of unique properties. First, the level structure decomposes into singlet and triplet states, with broad transitions within each system and narrow intercombination lines between them. Just as in the helium atom, the lowest triplet states are metastable. Second, states with zero electronic angular momentum are free of hyperfine structure. In addition, even-mass isotopes have even proton and even neutron numbers, leading to zero nuclear spin and absence of hyperfine structure in all electronic states. These properties enable a wealth of applications, including optical clocks [1], precision metrology [2], quantum computing [3–5], and Rydberg physics [6,7]. In recent years, AEM elements have played a major role in the search for yet undiscovered scalar gauge bosons through high-precision isotope shift spectroscopy [8], and various studies with neutral AEM atoms have been presented on this topic [9–14].

Alongside the AEM elements, and sharing these attractive properties, are the so-called group-IIB elements zinc, cadmium, and mercury. The broad singlet $^1S_0 \to {}^1P_1$ transitions for these elements lie deep in the ultraviolet range of the spectrum, with natural linewidths in excess of 100 MHz. They possess a multitude of even- and odd-mass isotopes, with the latter showing hyperfine structure. The resonance lines of the different isotopes are convoluted and often cannot be resolved in conventional Doppler-free spectroscopy. While Cd and Hg have already been employed for the development of optical clocks [15–17], there is very modest work towards this application with zinc thus far [18], mainly limited by the available laser technology. The wider chain of radioactive zinc isotopes is of interest for nuclear structure studies. For this reason, their isotope shifts have been measured in the triplet manifold [19,20], with new experiments ongoing [21,22].

Here, we present high-resolution spectroscopy of the $(4s^2)\,^1S_0 \to (4s4p)\,^1P_1$ transition near 213.8 nm in neutral zinc. Experiments were conducted over a two-week campaign in which an ultralow expansion cavity and required deep ultraviolet optics (University of Bonn) were transported to an atomic beam machine at the Fritz Haber Institute in Berlin. Our measurements are based on laser-induced fluorescence of a cryogenic beam of atoms extracted from a helium buffer gas cell. We employ a two-detector method to enable a clear distinction between even-mass isotopes with nuclear spin zero from the spin-5/2 ^{67}Zn isotope. As a result, we are able to use zinc samples of natural isotopic abundance in the experiments. Isotope shifts and hyperfine interaction constants are determined with an uncertainty of the order of 1 MHz. This method provides a blueprint for measurements of hyperfine structure in strong optical transitions, and a convenient and direct way to measure the true collection solid angle of a fluorescence detector. Our approach can be readily adapted to other species with several naturally occurring isotopes, e.g., Sn, Ni, and applied in the study of radioactive nuclei.

II. EXPERIMENTAL SETUP

Figure 1(a) illustrates our experimental apparatus and laser system. We use a cryogenic buffer gas source to produce a cold, slow atomic beam of zinc. The atoms are produced by laser ablation of a solid Zn target (natural abundance)

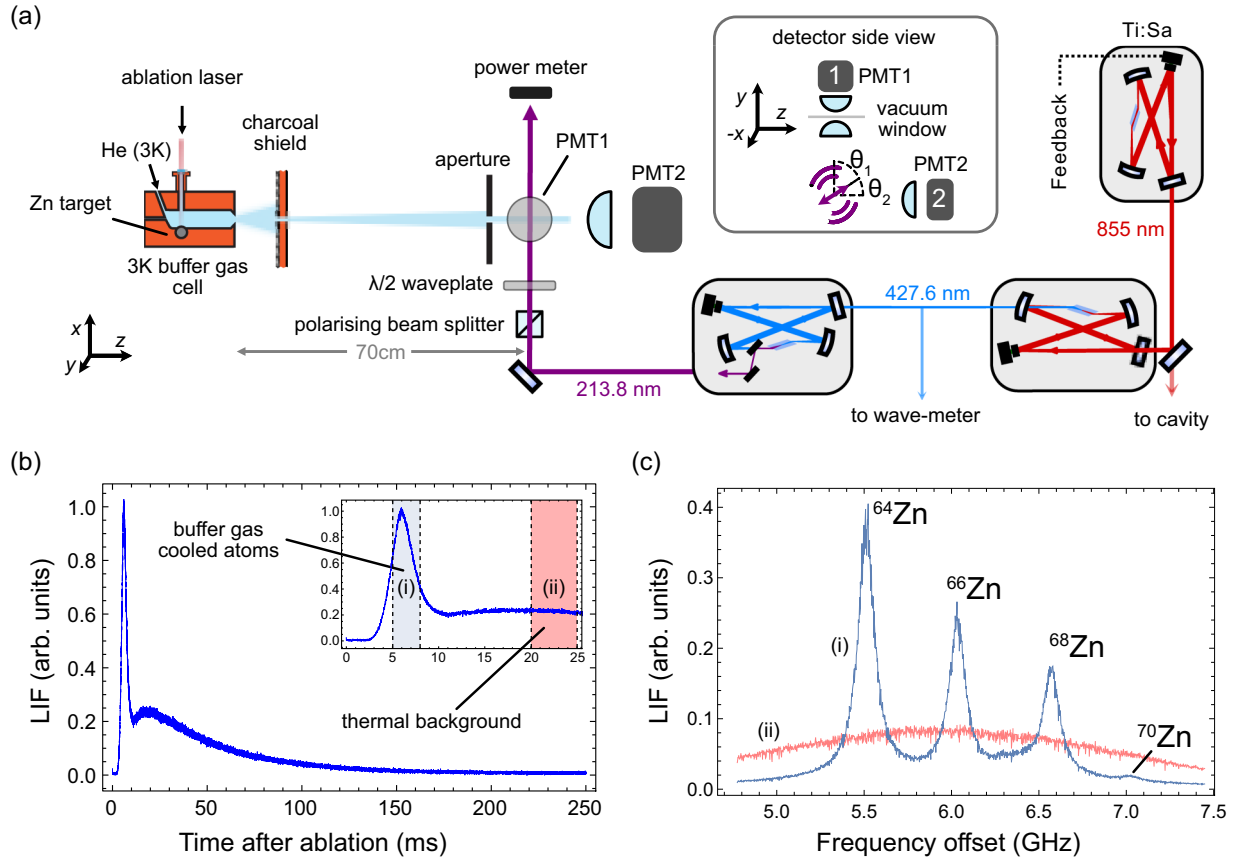*These authors contributed equally to this work.

†sidwright@fhi-berlin.mpg.de

FIG. 1. (a) Experimental setup for $^1S_0 \to \, ^1P_1$ laser-induced fluorescence spectroscopy of Zn, showing the cryogenic buffer gas beam, and 213.8 nm laser system. We also show a side view of the detector geometry, showing the two photomultipliers used, and the angles θ_1 and θ_2 relative to the linear polarization angle of the excitation light. These angles determine the emission pattern observed at the two detectors. (b) A typical time-of-flight fluorescence trace observed at the ^{64}Zn resonance. The inset shows a zoom-in of the region $0 < t < 25$ ms. Observation windows for the buffer gas cooled and thermal background components of the signal are shown by the shaded bars. (c) Fluorescence spectra for the observation windows in (b).

and are cooled in the cell by collisions with a He gas at a temperature of 3 K, and exit the cell with a typical velocity of 140 m/s along the z axis. The ablation laser is fired at a rate of 1 Hz which sets the repetition rate for the experiments. At a distance 70 cm downstream of the cell exit, we excite the $^1S_0 \to \, ^1P_1$ transition with a single probe laser beam near 213.8 nm, which intersects the atomic beam perpendicularly. A 2×2 mm square aperture restricts the range of transverse velocities in the atomic beam to below 2 m/s. Around 10^7 atoms per pulse pass through the detector.

Continuous wave laser light is produced by twice frequency doubling the infrared light of a Ti:sapphire laser near 855.2 nm. Each frequency doubling stage consists of an enhancement resonator containing a nonlinear crystal; to reach 213.8 nm from 427.6 nm, we use beta barium borate (β-BBO). The 855.2 nm light from the Ti:sapphire laser is frequency stabilized either by referencing to a commercial wave-meter (High Finesse WS8-10 calibrated with a temperature-stabilized HeNe laser) or via an ultralow expansion (ULE) optical cavity (Menlo ORC) with a measured free spectral range of 2.992 184(30) GHz. We also record the intermediate 427.6 nm light on the wave-meter since this light is immune from parasitic multimode content at the fundamental

wavelength. The wave-meter option offers an absolute accuracy of about 30 MHz when measuring the 427.6 nm light, a resolution of about 1 MHz, and enables continuous scanning over the entire spectrum. Scanning via the reference cavity reduces the linewidth of the laser and improves the linearity of the frequency axis. To do this, light at the fundamental wavelength of the Ti:sapphire laser is coupled into a fiber phase modulator (EOM, Jenoptik) driven with two rf frequencies, $\nu_{\text{PDH}} = 18$ MHz and $\nu_{\text{scan}} \sim 1$ GHz. The phase-modulated light reflected from the cavity is collected on a fast photodiode, demodulated at the frequency ν_{PDH} which produces a Pound-Drever-Hall (PDH) signal with sharp zero crossing points when the laser frequency is at a cavity resonance ν_c, or at $\nu_c \pm \nu_{\text{scan}}$. We lock the laser to the latter and scan the laser frequency by varying ν_{scan}. A camera is used to monitor the light transmitted through the cavity and ensure locking to the TEM$_{00}$ mode. This locking scheme enables continuous scanning of the Ti:sapphire laser frequency up to one-half of the cavity free spectral range, corresponding to 6 GHz at the 213.8 nm detection wavelength.

At the atomic beam machine, we purify the laser polarization with a polarizing beam cube and control its linear polarization angle relative to the direction of the atomic

beam with a $\lambda/2$ plate. The probe light propagates along the x axis and has a peak intensity $I = 10^{-3}I_{sat}$, where $I_{sat} = \pi hc\Gamma/(3\lambda^3) = 1.5\,\text{W/cm}^2$ is the two-level saturation intensity of the transition. Orthogonality between the laser and atomic beam direction is ensured using a set of alignment irises mounted on the detection chamber, and by aligning light through the atomic beam aperture and a small hole in the back of the buffer gas cell. We estimate that an atom traveling through the maximum intensity of the excitation light scatters five photons at resonance. The resulting laser-induced fluorescence (LIF) is collected and imaged onto two photomultiplier tubes (PMTs), whose photocurrents are delivered to separate transimpedance amplifiers and recorded as time-of-flight traces. The two PMTs are oriented to collect fluorescence emitted parallel and perpendicular to the direction of the atomic beam, as shown in Fig. 1(a). The angle θ_i between the laser polarization and the direction of detector i, illustrated in the inset to the figure, determines the portion of the fluorescence emission pattern collected by the two detectors. This enables discriminating between even- and odd-mass isotopes [13,23,24]. We record the laser power after the machine with a calibrated optical power meter and compensate for drifts in the probe intensity over a scan (typically 5–10%).

Figure 1(b) shows a typical time-of-flight trace observed in detector 1 when exciting the ^{64}Zn resonance. The signal comprises an initial intense peak from the buffer gas cooled atomic beam at roughly 5 ms, followed by an extended tail which appears for several tens of ms later. The extended tail consists of thermalized Zn atoms which leave the cell and collide with the vacuum walls without sticking; it persists even when the direct line of sight from the source to the detector is blocked, and leads to a broad background signal in the fluorescence spectra, whose Doppler width is consistent with the laboratory temperature. Example spectra showing the two signal components are shown in Fig. 1(c). Compared to a continuous atomic vapor source, signal from the thermalized atoms is significantly reduced simply by choosing an appropriate time-of-flight observation window.

III. ANALYSIS OF SPECTRAL LINE SHAPES

The five naturally occurring isotopes of zinc ($Z = 30$) can be separated into four even-mass isotopes and a single odd-mass isotope with mass number 67. In the following, we discuss the line-shape models used for these two cases in order to fit the experimental spectra. Here we use ν_L to label the laser frequency and assume that the laser linewidth is much less than the natural linewidth of the transition.

Line shape for even-mass isotopes. The even-mass zinc isotopes, all with nuclear spin $I_N = 0$, exhibit no hyperfine structure and the total angular momenta of the ground and excited states are $F = 0$ and $F' = 1$, respectively. The resonance line of an even-mass isotope e can be simply described with the line function,

$$S^{(e)} = \frac{\Gamma^2/4}{\Gamma^2/4 + \Delta_e^2}[1 - P_2(\cos\theta)g(\theta_C)]. \quad (1)$$

Here, $\Gamma/(2\pi)$ is the Lorentzian linewidth of the transition, $\Delta_e/(2\pi) = \nu_L - \nu_e$ is the detuning of the laser from the resonance frequency ν_e, and $P_2(\cos\theta) = \frac{1}{2}(3\cos^2\theta - 1)$ is the
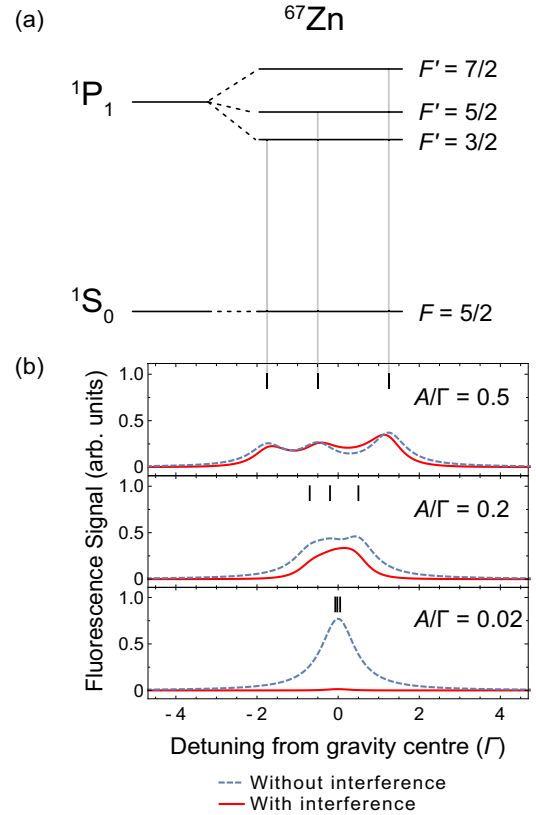

FIG. 2. Simulated fluorescence spectra for ^{67}Zn. (a) Level scheme labeling the total angular momenta F, F' for the ground and excited states, respectively. (b) Simulated spectra for detection along $\theta = 0$, for different values of the ratio A/Γ and with $B = 0$. We show the results with and without quantum interference included in the calculation. The sticks above the spectra correspond to the energies of the levels in (a). As A/Γ approaches zero (negligible hyperfine interaction), the emission pattern including interference converges to that of an ideal Hertzian dipole, meaning the emission is zero along $\theta = 0$.

second Legendre polynomial, with θ the angle between the detection direction and the electric field of the linearly polarized excitation light. The factor $g(\theta_C) = \cos(\theta_C)\cos^2(\theta_C/2)$ corrects for the effect of the finite solid angle of the detection optics, with θ_C the half angle of a circular collection lens. For $\theta = 0$, $S^{(e)} \to 0$ as $\theta_C \to 0$, as would be expected from the well-known Hertzian dipole radiation pattern. Importantly, adjusting θ or θ_C changes the amplitude of $S^{(e)}$ observed at the detector.

Line shape for odd-mass isotopes. There exists a single naturally abundant odd-mass isotope of Zn with nucleon number 67 and a nuclear spin $I_N = 5/2$. The nuclear spin couples with the electronic angular momentum J to give total angular momentum F, resulting in a single $^1S_0$, $F = 5/2$ hyperfine level and three $^1P_1$, F' excited levels with $F' = 3/2, 5/2, 7/2$. These energy levels are shown in Fig. 2(a). We assume the hyperfine energies $E(F)$ are given by

$$E(F) = \frac{A}{2}C + B\frac{\frac{3}{4}C(C+1) - I_N(I_N+1)J(J+1)}{2I_N(2I_N-1)J(2J-1)}, \quad (2)$$

with $C = F(F+1) - I_N(I_N+1) - J(J+1)$. Here, $A = A({}^1P_1)$ describes the strength of the magnetic dipole interaction between the electron and the nucleus. The coefficient $B = B({}^1P_1)$ describes the interaction strength between the nuclear electric quadrupole moment and the electric field gradient at the nucleus.

Following Brown *et al.* [25], the fluorescence spectrum of ^{67}Zn, $S^{(o)}$ can be separated into three terms:

$$S^{(o)} = \frac{\Gamma^2}{4}\{\mathcal{A} + [\mathcal{B} + \mathcal{C}]P_2(\cos\theta)g(\theta_C)\},$$

$$\mathcal{A} = \frac{1}{9}\left(\frac{2}{\Gamma^2/4 + \Delta_{3/2}^2} + \frac{3}{\Gamma^2/4 + \Delta_{5/2}^2} + \frac{4}{\Gamma^2/4 + \Delta_{7/2}^2}\right),$$

$$\mathcal{B} = -\frac{1}{225}\frac{1}{\Gamma^2/4 + \Delta_{3/2}^2}$$
$$- \frac{64}{525}\frac{1}{\Gamma^2/4 + \Delta_{5/2}^2} - \frac{2}{21}\frac{1}{\Gamma^2/4 + \Delta_{7/2}^2},$$

$$\mathcal{C} = \left[-\frac{8}{45}\frac{1}{(\Gamma/2 + i\Delta_{7/2})(\Gamma/2 - i\Delta_{3/2})}\right.$$
$$- \frac{6}{35}\frac{1}{(\Gamma/2 + i\Delta_{7/2})(\Gamma/2 - i\Delta_{5/2})}$$
$$\left.- \frac{1}{25}\frac{1}{(\Gamma/2 + i\Delta_{5/2})(\Gamma/2 - i\Delta_{3/2})}\right] + \text{c.c.} \quad (3)$$

Here, $\Delta_{F'}/(2\pi) = \nu_L - \nu_{F'}$ is the detuning of the laser from the excited state with total angular momentum F'; we assumed all Zeeman sublevels in the ${}^1S_0$ state are equally populated in the source and neglected optical pumping during the interaction with the probe light.

Important for the experiments is the fact that when the hyperfine structure is barely resolved, the emission pattern and hyperfine structure become strongly coupled. This is illustrated by Fig. 2(b), which shows simulated fluorescence spectra along $\theta = 0$ for different ratios of A/Γ. Each panel compares Eq. (3) with the result when interference is removed from the model, i.e., $\mathcal{C}$ is deliberately set to zero. The calculations show that as $A/\Gamma \rightarrow 0$, interference between scattering paths is destructive, leading to complete suppression of the fluorescence along this direction. There is an intuitive explanation for this effect: when the hyperfine interaction with the nucleus becomes negligible, the emission pattern must converge to that of the (spinless) even-mass isotopes. Conversely, one can produce the reverse effect in the even-mass isotopes by deliberately applying a magnetic field along $\theta = 90°$. This is the so-called Hanle effect [26,27] and, while understood for about a century, is often overlooked. The behavior illustrated in Fig. 2(b) shows that interference in the emission pattern of barely resolved lines contains useful information which can be used to constrain the hyperfine structure. The central spectrum in the figure, where $A/\Gamma = 0.2$, is near the value observed in the experiments. This results in a total span of the ${}^1P_1$ levels of $1.2\,\Gamma$, and reduces the peak scattering rate by about 40% with respect to that of the even-mass isotopes. Optical pumping between Zeeman sublevels of the ground state by the excitation light results in a time-dependent emission pattern, and a slight change to the fluorescence line shape. We simu-

lated population changes using rate equations and include this effect in our uncertainty analysis.

Combined line function. The total fit function used in this study is given by

$$S^{(\text{tot})} = a_{67}S^{(o)} + \sum_e a_e S^{(e)} + a_{bg}e^{-(\nu_L - \nu_{bg})^2/(2w_{bg}^2)}. \quad (4)$$

Here, a_{67} and a_e represent the relative abundances of the odd- and even-mass isotopes, respectively. The final term in Eq. (4) approximates the residual thermal background in the spectrum, whose amplitude a_{bg} is typically 5 to 10 percent of the ^{64}Zn resonance peak. The center frequency ν_{bg} and width parameter w_{bg} can be either fitted as free parameters or introduced as fixed parameters by first fitting the data at late arrival times when only the thermal background component is present. The fitted values for the isotope shifts in these two cases are consistent within the statistical error of the fits.

IV. RESULTS

A. Determination of the ^{67}Zn hyperfine structure by a two-detector method

Figures 3(a) and 3(b) show two sets of spectra obtained using the High Finesse wave-meter as a frequency reference. The data constitute two separate scans where the input polarization of the laser is along the y axis [Fig. 3(a)] and along the z axis [Fig. 3(b)], and for each panel, we show the fluorescence spectrum recorded by the two detectors 1 and 2. For clarity, each is labeled with a schematic showing the laser polarization, the detector orientation, and the dominant emission pattern for the even-mass isotopes. The different emission pattern of the ^{67}Zn isotope (relative natural abundance 4.1%) dramatically increases its visibility in detector i when $\theta_i = 0$. We show the fitted ^{67}Zn line shape with a black dashed line in each panel to illustrate this effect.

We use these spectra to determine solid angles of the collection optics and hyperfine structure of the ^{67}Zn isotope. The four spectra in Fig. 3 were fitted as a single dataset, fixing the detection angles θ_i to their values in the experiment, and enforcing the natural abundance of Zn isotopes [28]. This fixes the relative peak heights in each spectrum so that the detector solid angles $\theta_{C,1}, \theta_{C,2}$, and the hyperfine structure constants A and B of the ^{67}Zn isotope, can be determined. All resonance frequencies ν_e for all even-mass isotopes e, $\nu_{1/2,3/2,5/2}$ for the ^{67}Zn isotope, and a common Lorentzian linewidth Γ are shared fit parameters between the datasets. From this data, we conclude $\theta_{C,1} = 0.281 \pm 0.005$, $\theta_{C,2} = 0.145 \pm 0.005$ radians. The uncertainties are the range of values obtained when fitting the data with various reasonable assumptions, such as fixing the values of w_{bg} and ν_{bg} in the fit function using the signal at late arrival times. The value of $\theta_{C,2}$ is very close to the half angle subtended by the collection lens at the fluorescence region, 0.156(5) radians. The value of $\theta_{C,1}$ is significantly below the half angle subtended by its in-vacuum collection lens, 0.43(1) radians, and consistent with this lens being placed about 5 mm too close to the atomic beam, a result of incorrectly extrapolating the focal length from the visible to the deep ultraviolet.
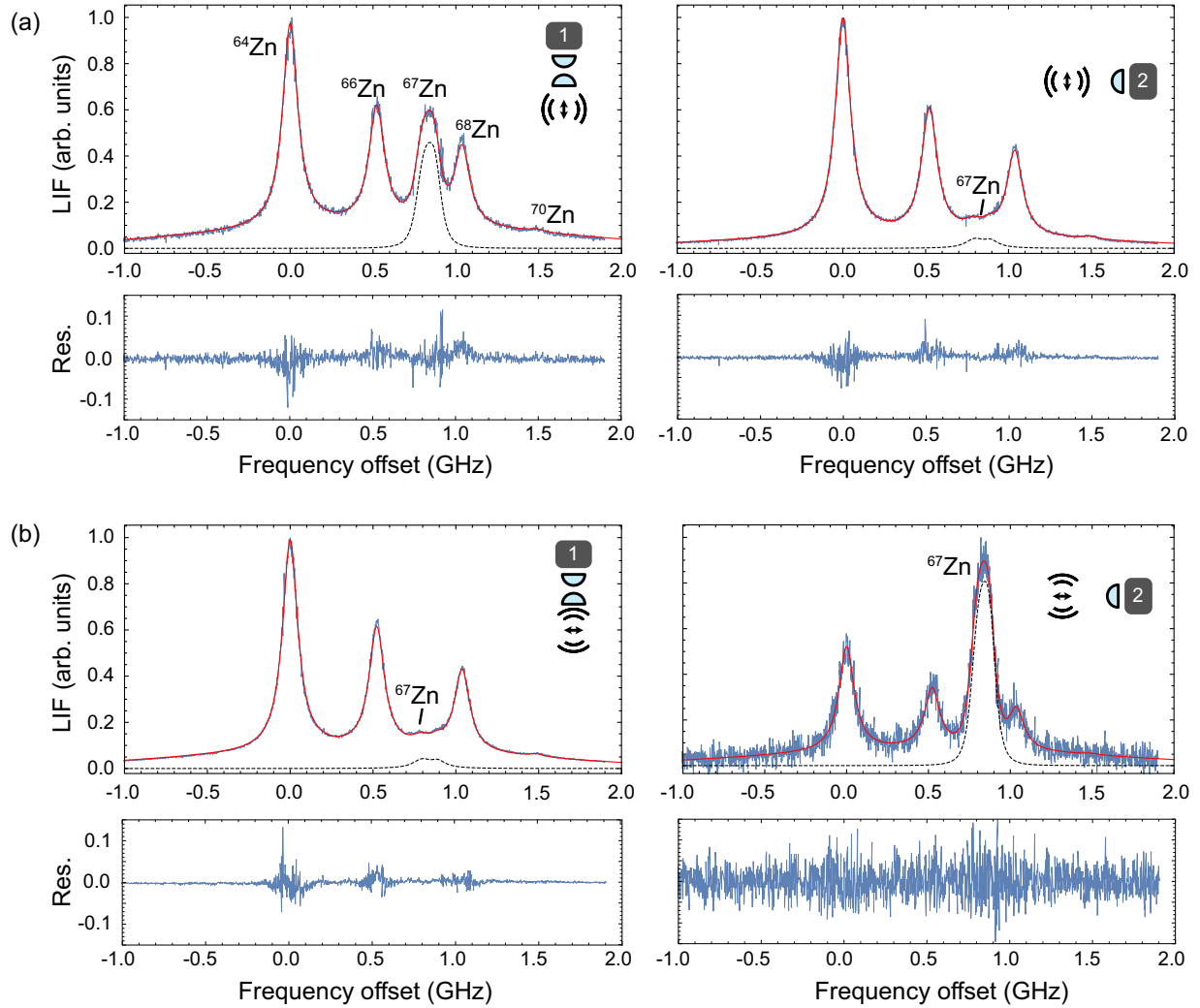
FIG. 3. Polarization sensitive fluorescence detection of Zn isotopes. Each spectrum is labeled by the probe laser polarization and detector configuration. The relative line intensities of the even- and odd-mass isotopes are strong functions of the angle θ between the laser polarization and the detector direction, and the solid angle of the collection optics. Blue lines show experimental data, red solid lines are fits as described in the text, and black dashed lines show the fitted ^{67}Zn line shape. Underneath each spectrum, the residuals are shown in a separate plot (Res). (a) Laser polarization along the y axis. (b) Laser polarization along the z axis.

For the hyperfine interaction parameters, we obtain $A(^{67}\text{Zn}) = 20 \pm 2\,\text{MHz}$ and $B(^{67}\text{Zn}) = 10 \pm 5\,\text{MHz}$. Fitting the data with $B = 0$ returns $A = 21\,\text{MHz}$ but noticeably reduces the goodness of the fit near the ^{67}Zn peak. Fitting to a model which ignores interference may be done by simply setting $\mathcal{C} = 0$ in Eq. (3); this gave the best-fit values $A = 9.5\,\text{MHz}$, $B = 0.6\,\text{MHz}$, $\theta_{C,1} = 0.37$, and $\theta_{C,2} = 0.20$, and line centers consistent with the full interference model. In this case, the fitted value of $\theta_{C,2}$ is larger than the geometric solid angle presented by the collection lens, and the fit residuals clearly indicate that only the interference model can adequately describe the signal observed in both detectors.

B. High-resolution measurements with the cavity

Having constrained the ^{67}Zn hyperfine structure and solid angle of the collection optics, we proceeded to scan the laser via the ULE reference cavity to more accurately determine the isotope shifts. Figure 4 shows spectra obtained when scanning ν_{scan} with the laser locked to the ULE cavity, and with the probe laser horizontally polarized. The scan rate corresponds to approximately 0.8 MHz/s for the 213.8 nm probe light, where the frequency ν_{scan} was measured near the time of the ablation laser pulse, and then stepped discretely after each measurement. By happenstance, the ^{66}Zn resonance appeared almost exactly at the midpoint between two cavity resonances, where the locking method fails. We therefore frequency shifted the Ti:sapphire laser light by 90 MHz before delivery to the cavity with an acoustic optic modulator, moving the unstable lock point by 360 MHz in the deep ultraviolet. The upper (lower) dataset in the figure is taken with (without) the frequency shifting method applied, on the same day but ablating different spots on the Zn target, which enabled measuring all isotopes. We fit the two spectra as a single dataset with shared resonance line positions in a Monte Carlo routine, where the values of $\theta_{C,1}$, $\theta_{C,2}$, A, and
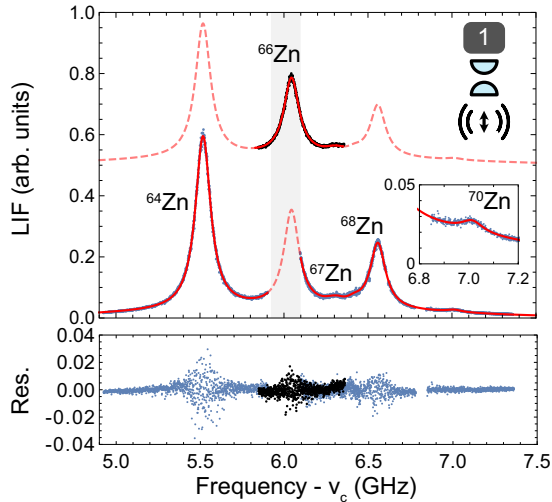
FIG. 4. Fluorescence spectra taken with the probe laser locked to the ULE cavity. The shaded box shows the region near the midpoint of the cavity resonances in which the lock fails. In the upper spectrum, shown with a deliberate offset on the *y* axis, the light delivered to the cavity was first frequency shifted by 90 MHz. This enables a continuous scan over the ^{66}Zn resonance. The two spectra are fitted as a single dataset to recover the isotope shifts as discussed in the text. Dashed lines show the fit functions where data are not present for each spectrum. The plot underneath shows the residual from the fit function for the two datasets.

B are drawn from uniform distributions whose ranges are given by the limits constrained in Sec. IV A. Enforcing the relative natural abundance of Zn in the fits leads to small changes in the best-fit values compared to allowing the line intensities to float, and we include this when estimating the uncertainties. We combine the best-fit values and errors for the isotope shifts to give a weighted mean and statistical error for these parameters, and assume a 1 MHz systematic frequency uncertainty which derives from the ∼200 kHz uncertainty of $\nu_{\rm scan}$ and the frequency shifting AOM, considering the two successive stages of frequency doubling. Doppler shifts due to slight misalignment of the probe laser light contribute an uncertainty ∼2 MHz to the absolute resonance frequencies, and negligibly to the isotope shifts. Recoil from absorption of the probe laser light leads to a Doppler shift of roughly 0.6 MHz across the detection volume, and the differential shift across the range of isotopes is an order of magnitude smaller. We neglect this contribution to the isotope shift uncertainty. The ambient magnetic field in the detector was measured as below 0.3 Gauss, corresponding to an upper bound to the line-shape broadening of 0.5 MHz.

V. DISCUSSION

Table I summarizes the results of our measurements and compares them to the available literature values. Our final values for the isotope shifts are presented relative to the ^{64}Zn resonance since this isotope is of highest abundance and its line center has the smallest statistical uncertainty. We combine measurements from the cavity and spectra taken using the wave-meter, and include a systematic frequency error of

TABLE I. Summary of the results obtained for the $(4s^2)\,^1S_0 \to (4s4p)\,^1P_1$ transition in Zn. Hyperfine constants and the radiative lifetime refer to the excited state. Results are given in MHz unless otherwise stated. CG: center of gravity. The isotope-averaged line center, $\bar{\nu}(^1S_0 - {}^1P_1)$, is computed as the average of the individual isotope line centers weighted by their isotopic abundance.

	This work	Literature
$\nu_{66} - \nu_{64}$	525.0(3.0)	480(60) [30]
		540(60) [31]
$\nu_{67}^{\rm (CG)} - \nu_{64}$	835(5)	
$\nu_{68} - \nu_{64}$	1039.8(1.7)	989(60) [30]
		960(85) [31]
$\nu_{70} - \nu_{64}$	1495(4)	
$A(^{67}$Zn$)$	20(2)	17.7(5) [29]
$B(^{67}$Zn$)$	10(5)	
$\nu_{64}/{\rm cm}^{-1}$	46745.394(2)	
$\bar{\nu}(^1S_0 - {}^1P_1)/{\rm cm}^{-1}$	46745.407(2)	46745.404(2) [32]
$\tau/{\rm ns}$	1.440(18)	1.40(3) [33]

2.1 MHz for the wave-meter values, which derives from directly comparing frequency intervals measured by the cavity scan method with the wave-meter. For the ^{67}Zn isotope shift, we increased the error bar by 1 MHz to account for the effect of optical pumping within the detection volume. Our values are two orders of magnitude more precise than previous measurements, also given in the table. Our value of $A(^{67}$Zn$)$ is consistent with the value measured by Kowalski and Träger [29], by level crossing spectroscopy of enriched ^{67}Zn. However, this study was unable to experimentally constrain the value of $B(^{67}$Zn$)$ and we therefore recommend the values from our measurements.

The absolute frequency of the ^{64}Zn resonance measured through our experiments is 1 401 391.66(6) GHz [46 745.394(2) cm^{-1}] and given in Table I. The uncertainty in our value is dominated by the wave-meter accuracy as specified by the manufacturer. The average of the line centers weighted by isotopic abundance, $\bar{\nu}(^1S_0 - {}^1P_1)$, is also given in the table. It is in excellent agreement with the (isotope-unresolved) hollow cathode lamp measurements presented in Ref. [32].

Our best-fit value of the Lorentzian linewidth is $\Gamma/(2\pi) = 110.5(1.4)$ MHz, where the error derives from the standard deviation of the Monte Carlo fitted values combined with the frequency uncertainty from the cavity scanning method. Fitting with a Voigt line shape did not change the value of Γ within the uncertainty of the fit, and returned a Gaussian contribution to the linewidth of 7(7) MHz full width at half maximum. The radiative lifetime $\tau = 1/\Gamma$ given in the table is consistent with the weighted average of five measurements collated by Doidge [33], and is a factor of two more precise than previous measurements.

King plot. We combine our isotope shift results with values reported for the $^1S_0 \to {}^3P_1$ intercombination transition [34] on a King plot as follows. We calculate the reduced isotope shifts $\delta\bar{\nu}^{A,A'} = \delta\nu/\mu^{A,A'}$, with $\mu^{A,A'}$ the difference in the
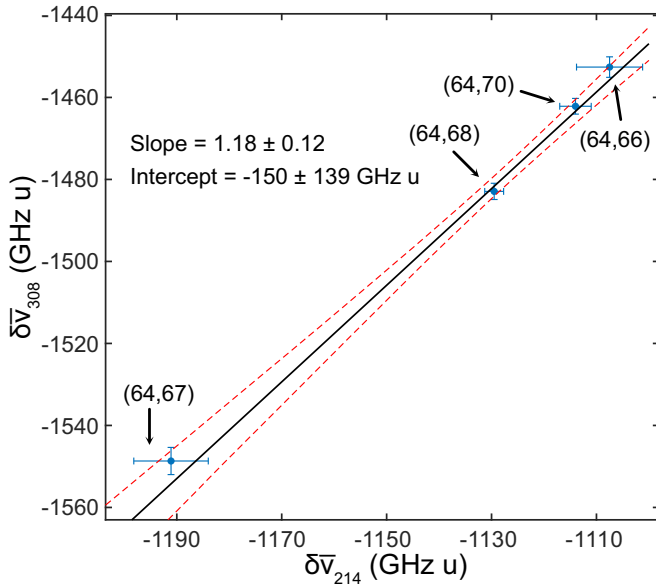
FIG. 5. A King plot of the $^1S_0 \to {}^1P_1$ (213.8 nm, this work) and $^1S_0 \to {}^3P_1$ (308 nm, Ref. [34]) transitions in Zn. The black solid line shows a linear fit to the data as discussed in the text. Red dashed lines indicate the 68% confidence interval of the fit.

inverse nuclear masses of the isotope pair (A, A'), and present the data in Fig. 5. The data are fitted to a linear relationship according to the recipe described in Ref. [35]. Briefly, we first define a mixing matrix to shuffle the 308 nm reduced isotope shifts so that they are referred to ^{64}Zn. We then calculate the covariance matrices, taking into account the mixing matrix and the reported errors. The most-probable values of the adjusted parameters, the intercept and slope, are found by minimizing a generalized χ^2 test statistic. To assign confidence intervals to the fitted parameters, we perform a Monte Carlo estimation procedure of repeated measurements drawn from a normal distribution centered at the most probable fitted values. The most probable value and 68% confidence interval of the fitted line is plotted in Fig. 5. That the value of the best-fitted slope, 1.18 ± 0.12, is close to 1 reflects the fact that the $(4s^2)^1S_0$ ground state is common to both transitions. The remaining field shift likely stems from electron correlation effects, contributing to small but non-negligible field shifts for the $4s4p$ states.

An additional hyperfine interaction between the different electronic states in Zn would additionally shift the gravity center of the ^{67}Zn resonance lines, $\nu_{67}^{(CG)}$, relative to the even-mass isotopes, and is often referred to as an "off-diagonal" hyperfine interaction. Such shifts should be detectable in a King plot as deviations of isotopes with nuclear spin from linear fits to the data of spin-zero isotopes (see, for example, Ref. [9]). To test for this, we repeat the fitting procedure without the (64,67) pair, and calculate its predicted values in each iteration of the Monte Carlo procedure to obtain its distribution. The resulting 68% confidence interval for the frequency difference $\nu_{67}^{(CG)} - \nu_{64}$ is from 818 to 834 MHz, which agrees with our measured value [835(5) MHz] within its uncertainty. We infer that the difference in off-diagonal hyperfine shifts of the ^{67}Zn resonances, for this pair of transitions, is less than 10 MHz.

This closely follows results of isotope shift measurements for the lowest lying, and analogous, transitions in cadmium [13], another group-IIB element. It may be of interest considering recently observed strong hyperfine mixing effects for higher-lying transitions in zinc in the collinear resonance ionization spectroscopy (CRIS) experiment [22].

VI. SUMMARY AND OUTLOOK

We have reported isotope shifts, radiative lifetime, and hyperfine structure measurements for the $(4s^2)^1S_0 \to (4s4p)^1P_1$ transition in neutral Zn by cw laser-induced fluorescence spectroscopy of an atomic beam. Our measurements considerably improve upon the published literature for this transition and contribute to the study of the ^{67}Zn nucleus, where unexpected isotope shifts have recently been observed in collinear laser spectroscopy at the ISOLDE facility [22]. With its multitude of nuclear spin-zero isotopes and various narrow optical transitions, zinc is a candidate for further isotope shift spectroscopy at the sub-kHz level.

The two-detector method and analysis procedure described here takes greater advantage of the information available in atomic fluorescence measurements and has several benefits. First, it enables reliably extracting hyperfine parameters from barely resolved peaks. Second, two spectra are obtained simultaneously in which the visibility of isotopes can be tuned based on their fluorescence emission pattern. This approach allows disentangling otherwise overlapping lines and, in the case of atomic Zn studied here, enables a measurement of the isotope shifts and hyperfine structure at the ~1 MHz level. The approach can readily be adopted to other elements which feature broad transitions and many isotopes. It may be of benefit for accelerator-based collinear laser spectroscopy experiments, in particular those involving nuclear isomers which are difficult to separate by nuclear mass (see, for example, Ref. [36]). In addition, there are often multiple fluorescence decay channels from a given excited state, to final states with different values of the angular momentum J. Isolating fluorescence from specific decay path with a spectral filter necessarily selects a specific emission pattern for each isotope, a further tool in spectral analysis.

ACKNOWLEDGMENTS

[1] A. D. Ludlow, M. M. Boyd, J. Ye, E. Peik, and P. O. Schmidt, Rev. Mod. Phys. **87**, 637 (2015).

[2] M. G. Tarallo, T. Mazzoni, N. Poli, D. V. Sutyrin, X. Zhang, and G. M. Tino, Phys. Rev. Lett. **113**, 023005 (2014).

[3] A. J. Daley, M. M. Boyd, J. Ye, and P. Zoller, Phys. Rev. Lett. **101**, 170504 (2008).

[4] A. V. Gorshkov, A. M. Rey, A. J. Daley, M. M. Boyd, J. Ye, P. Zoller, and M. D. Lukin, Phys. Rev. Lett. **102**, 110503 (2009).

[5] M. Saffman, J. Phys. B: At. Mol. Opt. Phys. **49**, 202001 (2016).

[6] C. E. Simien, Y. C. Chen, P. Gupta, S. Laha, Y. N. Martinez, P. G. Mickelson, S. B. Nagel, and T. C. Killian, Phys. Rev. Lett. **92**, 143001 (2004).

[7] A. Browaeys and T. Layahe, Nat. Phys. **16**, 132 (2020).

[8] J. C. Berengut, D. Budker, C. Delaunay, V. V. Flambaum, C. Frugiuele, E. Fuchs, C. Grojean, R. Harnik, R. Ozeri, G. Perez, and Y. Soreq, Phys. Rev. Lett. **120**, 091801 (2018).

[9] H. Miyake, N. C. Pisenti, P. K. Elgee, A. Sitaram, and G. K. Campbell, Phys. Rev. Res. **1**, 033113 (2019).

[10] M. Witkowski, G. Kowzan, R. Munoz-Rodriguez, R. Ciuryło, P. S. Żuchowski, P. Masłowski, and M. Zawada, Opt. Express **27**, 11069 (2019).

[11] N. L. Figueroa, J. C. Berengut, V. A. Dzuba, V. V. Flambaum, D. Budker, and D. Antypas, Phys. Rev. Lett. **128**, 073001 (2022).

[12] K. Ono, Y. Saito, T. Ishiyama, T. Higomoto, T. Takano, Y. Takasu, Y. Yamamoto, M. Tanaka, and Y. Takahashi, Phys. Rev. X **12**, 021033 (2022).

[13] S. Hofsäss, J. E. Padilla-Castillo, S. C. Wright, S. Kray, R. Thomas, B. G. Sartakov, B. Ohayon, G. Meijer, and S. Truppe, Phys. Rev. Res. **5**, 013043 (2023).

[14] B. Ohayon, S. Hofsäss, J. E. Padilla-Castillo, S. C. Wright, G. Meijer, S. Truppe, K. Gibble, and B. K. Sahoo, New J. Phys. **24**, 123040 (2022).

[15] A. Yamaguchi, M. S. Safronova, K. Gibble, and H. Katori, Phys. Rev. Lett. **123**, 113201 (2019).

[16] L. D. Sarlo, M. Favier, R. Tyumenev, and S. Bize, J. Phys.: Conf. Ser. **723**, 012017 (2016).

[17] R. Tyumenev, M. Favier, S. Bilicki, E. Bookjans, R. L. Targat, J. Lodewyck, D. Nicolodi, Y. L. Coq, M. Abgrall, J. Guéna, L. D. Sarlo, and S. Bize, New J. Phys. **18**, 113002 (2016).

[18] M. Büki, D. Röser, and S. Stellmer, Appl. Opt. **60**, 9915 (2021).

[19] C. Wraith, X. Yang, L. Xie, C. Babcock, J. Bieroń, J. Billowes, M. Bissell, K. Blaum, B. Cheal, L. Filippin, R. Garcia Ruiz, W. Gins, L. Grob, G. Gaigalas, M. Godefroid, C. Gorges, H. Heylen, M. Honma, P. Jönsson, S. Kaufmann *et al.*, Phys. Lett. B **771**, 385 (2017).

[20] L. Xie, X. Yang, C. Wraith, C. Babcock, J. Bieroń, J. Billowes, M. Bissell, K. Blaum, B. Cheal, L. Filippin, K. Flanagan, R. Garcia Ruiz, W. Gins, G. Gaigalas, M. Godefroid, C. Gorges, L. Grob, H. Heylen, P. Jönsson, S. Kaufmann *et al.*, Phys. Lett. B **797**, 134805 (2019).

[21] X. Yang, T. Cocolios, and S. Geldhof, Probing the magicity and shell evolution in the vicinity of $n = 50$ with high-resolution laser spectroscopy of ^{81,82}Zn isotopes (2020), CERN-INTC-2020-064 (unpublished).

[22] Y. Liu, X. Yang, S. Bai, J. Reilly, T. Cocolios, K. Flanagan, R. G. Ruiz, F. Gustafsson, J. Li, M. Ma *et al.*, *Collinear resonance ionization spectroscopy of stable 64, 66, 67, 68, 70 Zn isotopes* (2022), ISOLDE workshop and users meeting, Contribution ID: 21 (unpublished).

[23] W. Rasmussen, R. Schieder, and H. Walther, Opt. Commun. **12**, 315 (1974).

[24] P. E. G. Baird, R. J. Brambley, K. Burnett, D. N. Stacey, D. M. Warrington, and G. K. Woodgate, Proc. R. Soc. London. Ser. A, Math. Phys. Sci. **365**, 567 (1979).

[25] R. C. Brown, S. Wu, J. V. Porto, C. J. Sansonetti, C. E. Simien, S. M. Brewer, J. N. Tan, and J. D. Gillaspy, Phys. Rev. A **87**, 032504 (2013).

[26] W. Hanle, Naturwissenschaften **11**, 690 (1923).

[27] A. C. G. Mitchell and M. W. Zemansky, *Resonance Radiation and Excited Atoms* (Cambridge University Press, London, 1961), Chap. V.

[28] K. J. R. Rosman and P. D. P. Taylor, Pure Appl. Chem. **70**, 217 (1998).

[29] J. Kowalski and F. Träger, Z. Phys. A **278**, 1 (1976).

[30] M. Crawford, A. Schawlow, W. Gray, and F. Kelly, Can. J. Res. **28a**, 138 (1950).

[31] G. Hately and T. Littlefield, J. Opt. Soc. Am. **48**, 851 (1958).

[32] D. Gullberg and U. Litzén, Phys. Scr. **61**, 652 (2000).

[33] P. Doidge, Spectrochimica Acta Part B: Atom. Spectrosc. **50**, 209 (1995).

[34] P. Campbell, J. Billowes, and I. S. Grant, J. Phys. B: At., Mol. Opt. Phys. **30**, 2351 (1997).

[35] B. K. Sahoo and B. Ohayon, Phys. Rev. Res. **5**, 043142 (2023).

[36] P. Plattner, E. Wood, L. A. Ayoubi, O. Beliuskina, M. L. Bissell, K. Blaum, P. Campbell, B. Cheal, R. P. de Groote, C. S. Devlin, T. Eronen, L. Filippin, R. F. G. Ruíz, Z. Ge, S. Geldhof, W. Gins, M. Godefroid, H. Heylen, M. Hukkanen, P. Imgram *et al.*, Phys. Rev. Lett. **131**, 222502 (2023).